JCTC Journal of Chemical Theory and Computation

pubs.acs.org/JCTC Article

Coupling Solvation Thermodynamics and Chemical Speciation: A Simulation-Based Approach to NO_x Uptake in Aqueous Environments

Tijin H. G. Saji, Thijs J. H. Vlugt, Sofia Calero, and Behnaz Bagheri*

Cite This: J. Chem. Theory Comput. 2026, 22, 528−539 Read Online

ACCESS | Metrics & More | Article Recommendations | Supporting Information

ABSTRACT: We present a simulation-based framework to characterize the solvation and aqueous-phase reactivity of nitric oxide (NO) and nitrogen dioxide (NO_2) in water. Using Continuous Fractional Component Monte Carlo (CFCMC) simulations, we compute Henry coefficients and chemical potentials of NO and NO_2, while molecular dynamics (MD) simulations provide diffusion coefficients for NO. The results for NO are quantitatively in agreement with the experimental data when using the Saji force field. For NO_2, we model the chemical equilibrium involving hydrolysis and acid−base reactions that generate HNO_2, HNO_3, NO_2^-, NO_3^-, and H_3O^+. By combining the chemical potentials obtained via CFCMC with a thermodynamic equilibrium model, we resolve the temperature- and pressure-dependent speciation and pH of the system. The model captures a transition from nitrous to nitric species with increasing temperature and predicts ionic distributions and pH shifts under varying NO_x gas fluxes. This work provides a transferable methodology to connect molecular simulations with chemical speciation in reactive aqueous systems.

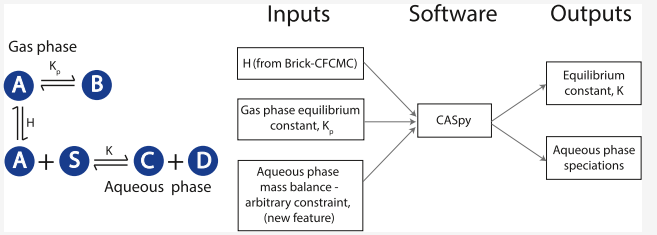

1. INTRODUCTION

Plasma technology is increasingly recognized as a versatile and sustainable platform for chemical transformations in agriculture and health care.[1−7] Plasmas are ionized gases generated by applying electricity to a feed gas, producing a mixture of charged and neutral species, radicals, and excited species that can drive a wide range of reactions.[8,9] When plasmas interact with liquids such as water, they produce a rich spectrum of reactive species that dissolve into the liquid phase.[8,9] By selecting different feed gases (for example, air or mixtures of N_2 and O_2 with inert gases such as Ar or He), plasma-water systems can be tailored to generate a specific mixture of reactive oxygen and nitrogen species (RONS) or other chemical intermediates in the aqueous phase.[8] This makes plasma technology a promising tool for sustainable agriculture and medical applications. In biomedical applications, RONS can be selectively delivered to living tissues to treat chronic wounds, skin infections, and certain cancers.[10−14] In agriculture, specific mixtures of RONS, applied directly or dissolved in water, can serve as fertilizers or pesticides to promote plant growth and health.[15−17]

For these applications, having control over the composition of RONS in the liquid phase is crucial. The aqueous chemistry in plasma-water systems is influenced by multiple parameters such as the type and composition of the feed gas, the properties of the electrical power source (e.g., voltage frequency and waveform), the geometry of the system, plasma exposure time, and the properties of the liquid, such as pH, permittivity, conductivity, and temperature. Understanding and tuning these parameters are essential to optimize the formation of a desired blend of RONS for specific purposes.[8]

Investigating plasma-water systems presents significant challenges due to their highly dynamic and coupled nature. Even for a fixed feed gas, power source, system geometry, and initial liquid properties, the plasma and liquid continuously evolve over time, influencing each other. This interplay makes experimental diagnostics of plasma-water systems extremely challenging.[8] Computational studies of plasma-water systems can provide valuable information by predicting and analyzing the formation of reactive species in the gas-phase plasma and its transport to the liquid phase.[18−24] Ideally, one would aim for a comprehensive, time- and space-resolved model that couples gas-phase plasma dynamics with liquid-phase chemistry. Such a model could predict the formation of species in both phases and their dependence on system parameters such as voltage, frequency, and waveform of the applied electrical power.[8] Achieving this requires a multiscale computational platform, as contrasting regimes of physics and chemistry hold on each side of the plasma-water interface. The classical

Received: October 13, 2025
Revised: December 20, 2025
Accepted: December 22, 2025
Published: December 29, 2025

behavior of electrons dominates in the gas-phase plasma, whereas quantum effects govern the interactions in the liquid phase. These two phases also have dramatically different electron densities as well as characteristic length and time scales.[25] Common computational approaches to plasma-water systems focus on a specific aspect of the system under certain assumptions, often using continuum models.[18−24] In these models, liquid properties are treated implicitly, or phenomenological parameters such as Henry coefficients are used to model the transport of species into the aqueous phase. As such parameters are known only for a limited set of species and conditions, the predictive power of continuum models of plasma-water systems remains limited. Molecular simulations are a natural choice for computing quantities such as solubility coefficients for plasma species.

In this work, we focus on modeling the absorption of nitric oxide (NO) and nitrogen dioxide (NO_2) into water using force field-based molecular simulations. NO and NO_2 are key species as part of the reactive nitrogen species (RNS) produced in the gas phase plasma,[26−30] which have biological significance.[31,32]

NO is a hydrophobic species with low solubility in water and is absorbed by water without undergoing reactions. We therefore consider system (a) in Figure 1 where NO in the gas phase is in physical equilibrium with NO in the liquid phase. We use Continuous Fractional Component Monte Carlo (CFCMC) simulations[33−35] to compute excess chemical potentials and consequently Henry coefficients of NO at temperatures ranging from 273 to 333 K. Furthermore, we use Molecular Dynamics (MD) simulations to calculate the self-diffusion coefficients of NO in water containing mole fractions of 0.005, 0.015, 0.025 NO at temperatures ranging from 273 to 333 K. We use our previously developed force field for NO[36] in combination with the TIP3P force field[37] to compute Henry coefficients and with the TIP4P/2005[38] to calculate self-diffusion coefficients. By comparing the results with the experimental values[39,40,40−43] we reflect on the verification and validity of our force field for NO in combination with the TIP3P[37] and the TIP4P/2005[38] force fields for water.

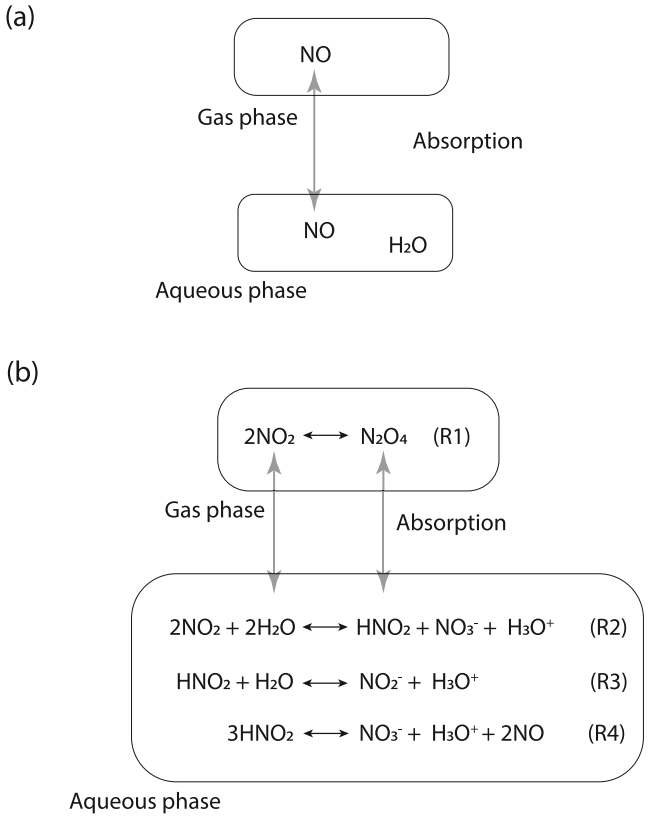

Figure 1. Schematic representation of (a) absorption of NO in water and (b) absorption of NO_2 and N_2O_4 in water with the subsequent equilibrium reactions involved.

NO_2 undergoes a dimerization reaction at ambient conditions and forms N_2O_4 in the gas phase. Furthermore, NO_2 undergoes chemical reactions with water. We consider system (b) in Figure 1 in which the dimerization reaction occurs in the gas phase (i.e., reaction R1). NO_2 and N_2O_4 are in physical equilibrium with their counterparts in the aqueous phase. Upon absorption of NO_2 in water, a hydrolysis reaction occurs to form nitrous acid (HNO_2) and nitric acid (HNO_3)[44−48] through reaction R2. Since HNO_3 is a strong acid,[49] we assume the complete dissociation of HNO_3 in water to give nitrate (NO_3^-) and hydronium (H_3O^+) ions. We incorporate the partial dissociation of HNO_2 to form nitrite ions (NO_2^-) and H_3O^+ through reaction R3 because HNO_2 is a relatively weak acid compared to HNO_3. HNO_2 can also dissociate to form HNO_3,H_2O, and NO through reaction R4. Note that we do not include the evaporation of water into the gas phase, as we study the system at temperatures in the range of 273 to 333 K, which is well below the boiling point of water. In addition, we do not include the dissociation of NO_2 to form NO and O_2 in the gas phase, as this reaction is not favorable at the temperatures and pressures we consider in this work.[46,50] Since our study focuses on the thermodynamic equilibrium of the system, transient species such as N_2O_3 or its isomer ONONO[46] are not considered, as they are thermodynamically unstable. We use CFCMC simulations[33−35] to compute the excess chemical potentials and, consequently, the Henry coefficients of the species involved. We calculate the isolated molecule partition functions of these species and therefore the standard-state ideal gas chemical potential. Finally, using these data, we determine the chemical composition (i.e., speciations) at a given gas-phase composition at total gas pressures ranging from 10^{-7} kPa to 10^2 kPa and at temperatures ranging from 273 to 333 K using the CASpy chemical reaction equilibrium solver.[51] We provide information on how the properties of water are altered when a specific flux of NO_2 and N_2O_4 species reaches the interface.

The data generated in this work have potential applications in continuum simulations of plasma-water systems, where data on plasma species is currently limited. The impact of this study extends beyond plasma technology, as NO_x species play key roles in numerous chemical processes in both nature and industry. Examples include atmospheric chemistry, where NO_x species are produced by lightning in air,[52,53] aerosol chemistry,[54] gas separation and purification processes in industrial applications.[55]

The remainder of the manuscript is organized as follows. The methods are described in Section 2. We discuss the results of the NO-water system (system (a) in Figure 1) in Section 3.1 and those of the NO_2-water system (system (b) in Figure 1) in Section 3.2. We compare our results with the available data in the literature where possible. Finally, concluding remarks are presented in Section 4.

https://doi.org/10.1021/acs.jctc.5c01718
J. Chem. Theory Comput. 2026, 22, 528−539

2. METHODOLOGY

2.1. Force Fields. In this work, all the species studied were modeled using all-atom classical nonpolarizable force fields. The Coulombic potential energy function is considered for the electrostatic interactions, and the 12−6 Lennard-Jones (LJ) potential energy function is considered for the van der Waals interactions. The Lorentz−Berthelot[56] mixing rules were used for the vdW interactions of unlike atoms. A cutoff radius of 12.5 Å was used for both the Lennard-Jones and Coulombic interactions. The Ewald summation method[57,58] was used to treat long-range Coulombic interactions. The energies and pressures were corrected with long-range tail corrections for the LJ interactions.[59]

For NO, we used our previously developed force field (Saji FF),[36] where NO is considered as a rigid molecule. The partial charges and the LJ parameters are presented in Table S8 of the Supporting Information. The force fields for NO_2 and its dimer N_2O_4 were taken from the work of Bourasseau et al.[60] NO_2 is treated as a rigid molecule. N_2O_4 is also treated as a rigid molecule except for the torsion about the N−N bond.[61] The torsion potential coefficients, partial charges, and the LJ parameters are provided in Tables S1 and S2 of the Supporting Information, respectively.

For H_3O^+ ions, the force field developed by Noroozi and Smith.[62] was used where the H_3O^+ is considered to be a rigid ion. The parameters of the potential energy functions of H_3O^+ are provided in Table S3. For HNO_2, NO_2^-, and NO_3^-, the force fields developed by Cordeiro et al.[63] are used. In the original work by Cordeiro et al.,[63] the bending potential energy functions of HNO_2, NO_2^-, and NO_3^- are described using the cosine-based angle potential function, which is of the form

$$E_{\text{bend}}(\theta) = \frac{1}{2}k^{\theta}(\cos(\theta) - \cos(\theta^0))^2 \tag{1}$$

where θ is the bond angle and k^{θ} is the force constant. Since the software that is used to perform the CFCMC simulations in this work (Brick-CFCMC[35,64,65]) does not support the above bending potential, the cosine-based angle potential was fitted to the harmonic angle potential, which is of the form

$$E_{\text{bend}}(\theta) = \frac{1}{2}k(\theta - \theta^0)^2 \tag{2}$$

where θ is the bond angle and k is the force constant of the harmonic angle potential. The force constant in the harmonic potential (k) is related to the force constant in the cosine-based potential (k^{θ})

$$k = k^{\theta}\sin^2(\theta^0) \tag{3}$$

The parameters and coefficients of the potential energy functions of NO_2^-, NO_3^- and HNO_2 are provided in Tables S4−S7 of the Supporting Information. Figure S10 of the Supporting Information shows a comparison of the harmonic and cosine-based angle potential functions for HNO_2 molecule. At room temperature (300 K), the thermal energy (k_BT) is approximately 2.5 kJ/mol. The deviation between the cosine-based potential and its harmonic approximation becomes significant only at energies above 200 kJ/mol, which corresponds to angular changes far larger than those sampled under thermal fluctuations in our simulations. Therefore, within the energy range relevant to our study, the harmonic approximation accurately reproduces the cosine-based potential. We note that in the original force field for NO_3^- developed by Cordeiro et al.,[63] an improper dihedral term is defined with an equilibrium angle of 0°, restricting the molecule to the planar geometry. In our simulations, the NO_3^- molecule is treated as a rigid body, which inherently fixes its internal geometry including planarity. As a result, the explicit inclusion of an improper dihedral term becomes redundant and is therefore neglected in our simulations.

The two water models used in this study are the TIP3P[37] and TIP4P/2005[38] models. In an earlier study, we showed that the TIP3P could predict the solubility of H_2O_2 molecule, which is also a plasma species, and the TIP4P/2005 could predict the self-diffusion coefficients of H_2O_2 molecule in good agreement with the experimental values.[66] We therefore used the TIP3P water model to calculate the Henry coefficients and the TIP4P/2005 to study the diffusion of NO in water. The interaction of all solutes with water in the NO_2-water system is modeled using the TIP3P water model.

2.2. MD Simulations. Molecular dynamics (MD) simulations were performed using the open-source large-scale atomic/molecular massively parallel simulator (LAMMPS).[67] The equations of motion are integrated with the Velocity-Verlet[59] algorithm, with a time step of 2 fs. Each system contained 1000 molecules in a simulation box of length 31 Å. The system is energy minimized using the conjugate gradient algorithm,[68] which is then followed by equilibration in the *NPT* ensemble for 10 ns. This is followed by an equilibration in the constant number of atoms/molecules, volume and temperature (*NVT*) ensemble for 5 ns. The production runs of 20 ns in the *NVT* ensemble were used to calculate thermodynamic properties such as viscosities and self-diffusivities using the OCTP[69] plugin in LAMMPS. The Nosé-Hoover thermostat[59,70,71] (with a coupling constant of 0.1 ps) and barostat (coupling constant of 1 ps) are used to keep the temperatures and pressure constant. Periodic boundary conditions were applied in all directions. The SHAKE algorithm is used to constrain the NO bond.

The self-diffusion coefficient (D_{MD}) is calculated from the mean-squared displacement of all molecules of species of interest[69]

$$D_{\text{MD}} = \lim_{t\to\infty} \frac{1}{2t}\frac{1}{3N_i}\left\langle \sum_{j=1}^{N_i} (\mathbf{r}_{j,i}(t) - \mathbf{r}_{j,i}(0))^2 \right\rangle \tag{4}$$

where t is the correlation time, N_i is the number of molecules of species i, and $\mathbf{r}_{j,i}$ is the position vector of jth molecule of species i. The viscosities are calculated from the autocorrelation function of all the components of the traceless stress tensor ($P^{\text{os}}_{\alpha\beta}$)[69]

$$\eta = \lim_{t\to\infty} \frac{1}{10\cdot 2t}\frac{V}{k_BT}\left\langle \sum_{\alpha\beta} \left(\int_0^t P^{\text{os}}_{\alpha\beta}(t')dt' \right)^2 \right\rangle \tag{5}$$

where V is the volume of the system. In eq 5, $P^{\text{os}}_{\alpha\beta}$ is given by

$$P^{\text{os}}_{\alpha\beta} = \frac{P_{\alpha\beta} + P_{\beta\alpha}}{2} - \delta_{\alpha\beta}\left(\frac{1}{3}\sum_k P_{kk}\right) \tag{6}$$

where $\delta_{\alpha\beta}$ is the Kronecker delta.

The self-diffusion coefficients were corrected for finite-size effects with the Yeh−Hummer equation[72,73]

$$D = D_{\text{MD}} + \frac{k_BT\xi}{6\pi\eta L} \tag{7}$$

https://doi.org/10.1021/acs.jctc.5c01718
J. Chem. Theory Comput. 2026, 22, 528−539

where D and D_{MD} denote the self-diffusion coefficient calculated with and without the finite-size effects corrections, respectively. k_B is the Boltzmann constant, T is the absolute temperature (in Kelvin), ξ is a dimensionless number which is equal to 2.837 for a cubic simulation box, L is the length of the cubic simulation box, and η is the viscosity of the system.

Three independent simulation runs were performed to obtain statistics, where each production run is divided into 2 blocks, giving 6 independent production blocks in total. The error bars are computed from the standard deviation of the 6 independent production blocks.

2.3. MC Simulations. Continuous Fractional Component Monte Carlo (CFCMC) simulations[33−35] using the open-source Brick-CFCMC software[35,64,65] were performed in the constant number of atoms/molecules, pressure and temperature (NPT) ensemble. In CFCMC simulations, fractional molecules (compared to the "whole" molecules) are introduced within the simulation system. The interactions of these fractional molecules are scaled using a continuous coupling parameter λ, the value of which ranges from 0 to 1. $\lambda = 0$ corresponds to the fractional molecule that acts as an ideal gas molecule and has no interactions with the other molecules of the system. $\lambda = 1$ means the fractional molecule is a whole molecule and has full interactions with the other molecules in the system. To ensure a flat observed probability distribution of λ, a bias is introduced using the Wang−Landau algorithm.[74] This biases the coupling parameter λ with a weight function $W(\lambda)$, thus ensuring the sampling issues due to energy barriers in λ space are not encountered. We used 100 bins to obtain a histogram for λ values and their probability of occurrence $p(\lambda)$. The Boltzmann average of an observable (A) is calculated using[75]

$$\langle A \rangle = \frac{\langle A \exp[-W(\lambda)] \rangle_{\text{biased}}}{\langle \exp[-W(\lambda)] \rangle_{\text{biased}}} \tag{8}$$

The excess chemical potential (μ^{ex}) is the difference between the total chemical potential and the ideal gas chemical potential of a molecule.[66] For small and/or weakly polar molecules, such as NO, NO_2, N_2O_4 and H_2O, μ^{ex} can be calculated from the ratio of the Boltzmann sampled probability distribution of λ at 1 ($p(\lambda = 1)$) and 0 ($p(\lambda = 0)$)

$$\mu_i^{ex} = -k_B T \ln\left[\frac{p(\lambda = 1)}{p(\lambda = 0)}\right] \tag{9}$$

Here, k_B is the Boltzmann constant and T is the absolute temperature. For large and/or strongly polar molecules, such as NO_2^-, NO_3^- and H_3O^+, $W(\lambda)$ can be large (>100 k_BT), making it difficult to obtain a flat observed probability distribution of λ, resulting in large uncertainties while computing μ_i^{ex} using eq 9. Thermodynamic integration is a viable alternative to compute μ^{ex} of large and/or strongly polar molecules as it does not require sampling of the full λ space with equal probability.[65] Instead, values of $\left\langle \frac{\partial U}{\partial \lambda} \right\rangle$ are computed from a series of independent simulations at different fixed values of λ for $\lambda \in [0, 1]$. Here, U is the total potential energy of the system. μ^{ex} is then computed by integrating $\left\langle \frac{\partial U}{\partial \lambda} \right\rangle$

$$\mu_i^{ex} = \int_0^1 \left\langle \frac{\partial U}{\partial \lambda} \right\rangle d\lambda \tag{10}$$

We note that thermodynamic integration is computationally more expensive than CFCMC simulations to compute μ^{ex}. Therefore, we only use the thermodynamic integration method to compute μ^{ex} of large and/or strongly polar species. As shown by Polat et al.,[65] both methods produce statistically equivalent results for small and neutral species. Consequently, for such systems we use CFCMC to calculate μ^{ex} with accuracy comparable to thermodynamic integration but at a significantly reduced computational cost. The Python script that was used to calculate the values of μ^{ex} for the NO_3^- + H_3O^+ system using thermodynamic integration is provided in the Supporting Information (the reader is also referred to Figure S16 therein). To maintain charge neutrality of the system, ionic species (an anion and a cation) are combined to form a fractional group[51,64] such that the total charge within the fractional group is zero.

The Henry volatility coefficient (K_v^{px}) in units of [Pa] is obtained from the excess chemical potential using[76]

$$K_v^{px} = \rho\, k_B T \exp\left(\frac{\mu^{ex,\infty}}{k_B T}\right) \tag{11}$$

where ρ is the number density of the solvent. The Henry coefficient (H_s^{cp}) in units of [mol/m^3 Pa] is obtained using the following conversion: $H_s^{cp} \approx \frac{\rho_{H_2O}}{M_{H_2O} K_v^{px}}$ in which ρ_{H_2O} is the density of water, and M_{H_2O} is the molar mass of water.[77] The Henry coefficient (H_s^{cp}) will have SI units only if ρ, k_B, T, and M are in SI units.

For Henry coefficient calculations, 5×10^6 equilibration cycles were performed. Five independent production runs of 3×10^6 cycles were performed to obtain statistics. Note that one cycle refers to N number of trial moves, where N is the total number of molecules. The error bars were calculated from the standard deviation of the 5 independent production runs.

2.4. Calculating Speciations. In this section, we describe the procedure by which we calculate the mole fraction of H_2O, NO_2, NO_2^-, N_2O_4, HNO_2, NO_3^-, H_3O^+, and NO in the aqueous phase for the NO_2-water system. The equilibrium constant of the dimerization reaction R1 in the gas phase is defined as $K_p = \left[\frac{P_{N_2O_4} P_0}{P_{NO_2}^2}\right]$, wherein P_{NO_2} and $P_{N_2O_4}$ are the partial pressures of NO_2 and N_2O_4, respectively. $P_0 = \rho_0 k_B T$, where ρ_0 is the reference number density taken as 1 molecule Å^{-3}. In the Supporting Information, we show that K_p can be written as follows

$$K_p = \exp\left[\frac{\mu^0_{N_2O_4} - 2\mu^0_{NO_2}}{-RT}\right] \tag{12}$$

where $\mu^0_{N_2O_4}$ and $\mu^0_{NO_2}$ are standard state ideal gas chemical potential of N_2O_4 and NO_2 molecules. R is the ideal gas constant. The composition of the gas phase for a particular total gas pressure (P_{total}) and temperature (T) can be calculated using the following relation

$$N_{N_2O_4}^2 + N_{N_2O_4} N_{NO_2} - \frac{N_{NO_2}^2 V_0 P_{total} K_p}{k_B T} = 0 \tag{13}$$

where $N_{N_2O_4}$ and N_{NO_2} are the number of molecules of N_2O_4 and NO_2, in the gas phase, respectively. V_0 equals 1 Å^3. The derivation of eq 13 is presented in the Supporting Information.

https://doi.org/10.1021/acs.jctc.5c01718
J. Chem. Theory Comput. 2026, 22, 528−539

The composition of the gas phase at total gas pressures ranging from 10^{-7} kPa to 10^{2} kPa and different temperatures (273, 298, 313, and 333 K) is listed in Table S10 of the Supporting Information. These values are in good agreement with reported values in the literature.[61,78]

We calculate the mole fraction of the six species in the aqueous phase such that the conservation of total charge and mass is satisfied via the following relations, whose derivations are provided in the Supporting Information

$$\begin{aligned} N_{H_2O} + 2N_{NO_3^-} - N_{NO} + N_{NO_2^-} &= 0 \\ N_{NO_3^-} - 2N_{NO} - N_{HNO_2} - N_{NO_2^-} &= 0 \\ N_{NO_3^-} + N_{NO_2^-} - N_{H_3O^+} &= 0, \end{aligned} \tag{14}$$

and the equilibrium of the reactions R2-R4 (see Figure 1) is attained via the following relation

$$\sum_{i=1}^{N_{species}} \nu_{i,j}\mu_i = 0 \tag{15}$$

where N_i indicates the number of a particular species i, $N_{species}$ is the total number of species involved (solutes and solvent) involved in the chemical reaction j, $\nu_{i,j}$ is the stoichiometric coefficient of the species i in the reaction j, and μ_i is the chemical potential of the species i. Note that the stoichiometric coefficients of the reaction products are considered positive, whereas those of the reactants are considered negative. We added a new functionality to the CASpy solver that allows users to define an arbitrary constraint for mass balances.

The chemical potential of a solute i, μ_i, using the ideal gas reference state, as used in Brick-CFCMC,[51,64] is

$$\mu_i = \mu_i^0 + RT \ln\left[\frac{\rho_i}{\rho_0}\right] + \mu_i^{ex} \tag{16}$$

where μ_i^0 is the standard state ideal gas chemical potential of solute i, as defined in the Brick-CFCMC software,[51,64] R is the ideal gas constant, T is the absolute temperature, ρ_i is the number density of solute i, ρ_0 is the reference number density, taken as 1 molecule Å^{-3}. μ_i^{ex} is the excess chemical potential of the solute i in the solvent, which is computed using eqs 9 or 10.

The chemical potential of the solvent (μ_s), as used in Brick-CFCMC,[51,64] is calculated using the ideal gas reference state

$$\mu_s = \mu_s^0 + RT \ln\left[\frac{\rho_{pure}}{\rho_0}\right] + \mu_s^{ex} - RT\left[\frac{1 - X_s}{X_s}\right] \tag{17}$$

where μ_s^0 is the standard state ideal gas chemical potential of the solvent, ρ_{pure} is the number density of the pure solvent, X_s is the mole-fraction of the solvent in the solution, and μ_s^{ex} is the excess chemical potential of the solvent, which is computed using eq 9. The fourth term, $RT\left[\frac{1-X_s}{X_s}\right]$, originates from the Gibbs–Duhem equation.[79] The value of this term is small as the mole fraction of the solvent (X_s) is close to unity.

By substituting eqs 16 and 17 in eq 15, and with some rearrangement, the following relation is obtained for each reaction j[51]

$$\begin{aligned} \prod_{i=1}^{N_{species}} X_i^{\nu_{i,j}} = & \exp\left[-\sum_{i=1}^{N_{species}} \frac{\nu_{i,j}(\mu_i^0 + \mu_i^{ex})}{RT}\right] \times \\ & \exp\left[-\nu_{s,j} \ln\left(\frac{\rho_{pure}}{\rho_0}\right)\right] \times \\ & \exp\left[\nu_{s,j}\left(\frac{1 - X_s}{X_s}\right)\right]\left[\frac{V\rho_0}{\sum_{i=1}^{N_{species}} N_i}\right]^{\nu_{tot\text{-}s,j}} X_s^{\nu_{s,j}}, \end{aligned} \tag{18}$$

where $\nu_{s,j}$ is the stoichiometric coefficient of the solvent in reaction j, N_i is the number of molecules of species i, and $\nu_{tot\text{-}s,j}$ is the sum of stoichiometric coefficients of the solutes (all species except solvent) involved in reaction j. The left-hand side of eq 18 is the equilibrium constant of reaction j, K_j. The value of K_j can be exponentially large or exponentially small, therefore its natural logarithm $\ln[K]$ is often reported in the literature. Equations 14 and 18 are solved using an iterative procedure which is implemented in the open-source Python solver, CASpy.[51] To estimate the uncertainties of the $\ln[K]$ and mole fractions of species, we performed an error-propagation analysis based on Monte Carlo sampling. For each of the eight species, values of μ^{ex} were selected from Gaussian distributions whose means and standard deviations were taken from the computed values of μ^{ex} (see Table 3). These sampled values of μ^{ex} were used as input to CASpy, which then computed the corresponding $\ln[K]$ and mole fraction of species. A total of 20,000 Monte Carlo samples were generated. The resulting probability distribution of $\ln[K]$ and mole fractions of species were binned into histograms, to which Gaussian functions were fitted. The means and standard deviations obtained from these fitted Gaussian distributions were taken as the final uncertainties in $\ln[K]$ and mole fractions of species. This procedure was repeated for all four temperatures (273, 298, 313, and 333 K) of this study. The probability distributions as a function of $\ln[K]$ and mole fraction of species at 273 K at a total gas pressure of 10^1 kPa are shown as histograms in Figures S14 and S15 of the Supporting Information, respectively. The corresponding fits to a Gaussian distribution are also shown. The means and standard deviations of the mole fractions of species obtained using error propagation analysis at 273 K and at a total gas pressure of 10^1 kPa are listed in Table S17 of the Supporting Information.

The standard state ideal gas chemical potential, μ_i^0, is calculated using the isolated molecule partition function (q_{total}) of the species i using the relation

$$\mu_i^0 = -k_B T \ln\left[\frac{qV_0}{\Lambda^3}\right] \tag{19}$$

where q is the isolated molecule partition function of the system excluding the translation partition function, $q_{total} = \frac{qV_0}{\Lambda^3}$ where Λ is the thermal de Broglie wavelength of the species and $V_0 = 1$ Å^3 is a reference state for the translational part of the isolated molecule partition function in Brick-CFCMC software. The isolated molecule partition function is described extensively in our previous work[36] and in refs 51, 64. The required inputs to calculate the isolated molecule partition function of H_2O, NO_2^-, NO_3^-, HNO_2, and H_3O^+ are obtained from the JANAF tables[80] and the NIST database,[81] and are presented in Table S9 of the Supporting Information. To

https://doi.org/10.1021/acs.jctc.5c01718
J. Chem. Theory Comput. 2026, 22, 528−539

calculate the electronic contribution to the isolated molecule partition function of each species, atomization energy of that species is required. The atomization energy of the nitrate ions (D_{0,NO_3^-}) is not readily available and is calculated using the following equation

$$D_{0,NO_3^-} = D_{0,NO_3} + \text{E. A}(NO_3) \quad (20)$$

where D_{0,NO_3} and E.A(NO_3) are the atomization energy and electron affinity of NO_3 molecules, respectively. E.A(NO_3) is taken as 3.09 eV.[82] We calculated the value of $\ln\left[\frac{qV_0}{\Lambda^3}\right]$ as a function of temperature by writing it in the form of $\frac{A}{T} + B$. The values of parameters A and B for H_2O, NO_2^-, NO_3^-, HNO_2, and H_3O^+ are listed in Table 1. For NO species, the isolated molecule partition function is calculated using the parameters A and B provided in our previous work.[36] For NO_2 and N_2O_4 the parameters A and B provided by Lasala et al.[61] are used. The values of the standard-state ideal gas chemical potential, μ^0, for H_2O, NO_2, N_2O_4, HNO_2, NO_2^-, NO_3^-, H_3O^+, and NO at 273, 289, 313, and 333 K are listed in Table 2.

Table 1. Correlation Function for the Isolated Molecule Partition Function $\ln\left[\frac{qV_0}{\Lambda^3}\right]$ in the form of $\frac{A}{T} + B$ for H_2O, NO_2^-, NO_3^-, HNO_2, and H_3O^+[a]

	H_2O	NO_2^-	NO_3^-	HNO_2	H_3O^+
A	109485.30	157645.91	171511.92	149658.54	36727.67
B	11.11	15.35	17.66	18.36	11.57

[a]Here T is the temperature, and A and B are constants. The input data for calculating the isolated molecule partition function are obtained from the JANAF tables[80] and the NIST database,[81] and are listed in Table S9 of the Supplementary Information.

3. RESULTS AND DISCUSSION

3.1. NO-Water. *3.1.1. Self-Diffusion Coefficients.* The self-diffusion coefficients of NO for three different mole fractions of NO in water (0.005, 0.015, 0.025) at temperatures ranging from 273−333 K, were computed and are shown in Figure 2. D_{NO} increases with temperature for all the concentrations of NO. At a given temperature, values of D_{NO} for different concentrations of NO are close to each other (average difference of 4%). The computed values of D_{NO} are in excellent agreement with experimental values (Malinski et al.[41] at 298 K and Zacharia & Deen[40] at 310 K). The self-diffusion coefficients of water for these systems for the temperature range of 273 K−333 K are shown in Figure S8 of the Supporting Information, and are in good agreement with the self-diffusion coefficients of TIP4P/2005 water model. The viscosities of NO-water systems at different temperatures are given in Figure S9 of the Supporting Information. The systems with different mole fractions of NO have comparable viscosities as TIP4P/2005 water model for the temperature range of 273 K−333 K.

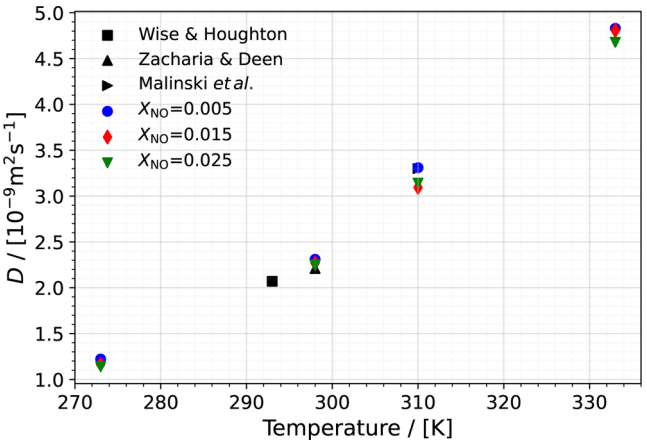

Figure 2. Self-diffusion coefficients of NO in NO-water systems for different mole fractions of NO (X_{NO}) in water (X_{NO} = 0.005, 0.015, 0.025) at different temperatures using the Saji et al.[36] force field model and the TIP4P/2005[38] water model. Error bars are estimated based on the standard deviation of 6 production blocks, and are much smaller than the symbols used in the figure. The experimental self-diffusion coefficients obtained from the work of Wise & Houghton,[39] Zacharia & Deen,[40] and Malinski et al.[41] are shown in black symbols.

3.1.2. Henry Coefficients. The computed values of μ^{ex} of NO for the temperature range 273 K - 333 K are listed in Table 3. Henry coefficients for NO (calculated from μ^{ex}) for the temperature range 273 to 333 K are shown in Figure 3. The Henry coefficients for NO (H_{NO}) decreases from 1.7 × 10^{-5} mol/m^3 Pa at 273 K to 1.45 × 10^{-5} mol/m^3 Pa at 298 K and remains approximately constant from 298 to 333 K. The experimental values of H_{NO} at 298 K from the work of Zacharia and Deen,[40] Zafiriou and McFarland,[42] and Komiyama and Inoue,[43] are also shown in the figure. The computed H_{NO} at 298 K is within the range of the reported experimental values.

From the results of Sections 3.1.1 and 3.1.2, we conclude that the force field which we developed for NO in our previous work[36] combined with the TIP4P/2005[38] and TIP3P water models[37] predicts the thermodynamic properties of NO in water in excellent agreement with experimental values. The computed values of μ^{ex} of NO are used in the next section for calculating the solubility of NO_2 in water and its speciation.

3.2. NO_2-Water. The values of μ^{ex} for H_2O, NO_2, N_2O_4, HNO_2, NO_3^- + H_3O^+, and NO at 273, 289, 313, and 333 K are presented in Table 3. Note that μ^{ex} of NO_3^- + H_3O^+ is calculated in a single simulation taking NO_3^- and H_3O^+ as a

Table 2. Values of the Standard State Ideal Gas Chemical Potential, μ^0 (as Defined in the Brick-CFCMC Software[51,64]), in Units of [kJ/mol] for the Species Studied in This Work for Different Temperatures[a]

T/[K]	H_2O	NO_2	N_2O_4	HNO_2	NO_2^-	NO_3^-	H_3O^+	NO
273	−935.51	−959.95	−1953.21	−1286.02	−1345.23	−1465.89	−331.63	−652.41
298	−937.79	−963.36	−1958.03	−1289.79	−1348.72	−1469.72	−334.02	−654.75
313	−939.18	−965.40	−1960.93	−1292.09	−1350.84	−1472.05	−335.47	−656.15
333	−941.06	−968.13	−1964.79	−1295.20	−1353.70	−1475.21	−337.44	−658.02

[a]The calculated values of μ^0 are in agreement with available literature data ($\mu^0_{H_3O^+,313\,K}$ = −338.21 kJ/mol[51]) within the chemical accuracy. These values are obtained using the input data presented in Table S9 of the Supplementary Information.

https://doi.org/10.1021/acs.jctc.5c01718
J. Chem. Theory Comput. 2026, 22, 528−539

Table 3. Computed Values of μ^{ex} for the Species Studied in This Work Using the TIP3P Water Model[37] for Different Temperatures in Units of kJ/mol[a]

T/[K]	H_2O	NO_2	N_2O_4	HNO_2	$NO_3^- + H_3O^+$	NO
273	$-26.97_{0.07}$	$4.98_{0.06}$	$-6.2_{0.1}$	$-16.0_{0.2}$	$-751.2_{0.1}$	$7.43_{0.09}$
298	$-25.66_{0.09}$	$6.17_{0.08}$	$-5.3_{0.1}$	$-14.9_{0.3}$	$-745.0_{0.2}$	$8.29_{0.05}$
313	$-24.91_{0.05}$	$6.68_{0.04}$	$-4.5_{0.1}$	$-14.2_{0.2}$	$-740.7_{0.2}$	$8.66_{0.03}$
333	$-23.99_{0.04}$	$7.30_{0.06}$	$-3.2_{0.1}$	$-13.6_{0.1}$	$-735.9_{0.2}$	$9.03_{0.04}$

[a]The standard deviations are given in subscripts. The computed values of μ^{ex} are in agreement with available literature data ($\mu^{ex}_{H_2O,298\,K} = -26.11$ kJ/mol[62]). Note that the μ^{ex} of $NO_3^- + H_3O^+$ is computed from 3 independent simulations taking NO_3^- and H_3O^+ as a single fractional group to maintain charge neutrality. μ^{ex} of $NO_2^- + H_3O^+$ is not computed as the equilibrium constant required for the reaction $HNO_{2(aq)} + H_2O_{(l)} \rightleftharpoons NO^-_{2(aq)} + H_3O^+(aq)$ were taken from ref 83

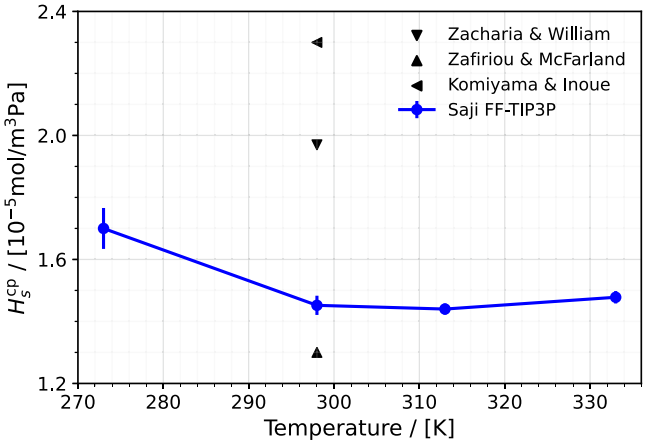

Figure 3. Henry coefficients for NO in water for temperatures ranging from 273 to 333 K using the Saji et al.[36] force field and TIP3P water model.[37] Error bars are estimated based on the standard deviation of 5 independent production runs. Experimental Henry coefficient of NO in water at 298 K is added for comparison.[40,42,43]

single fractional group to maintain charge neutrality. The μ^{ex} of $NO_2^- + H_3O^+$ is not calculated because the equilibrium constant required for the reaction R3 was taken from ref 83 μ^{ex} of all species increases with increasing temperature. NO and NO_2 have positive values of μ^{ex} while all other species have negative values of μ^{ex}. This indicates that NO and NO_2 are less hydrophilic compared to other species present in the system. The values of the Henry coefficients, H_s^{cp}, for H_2O, NO_2, N_2O_4, HNO_2, and NO at different temperatures are presented in Table 4. A higher value of H_s^{cp} indicates a higher solubility in water and therefore a higher hydrophilicity of the species. Species that are more hydrophilic (more negative values of μ^{ex}) have a higher value of H_s^{cp}. The computed value of H_s^{cp} for NO_2 differs by a factor of 2 to 3 compared to the existing experimental values (6.9×10^{-5}–1.2×10^{-4} mol/m^3 Pa at 298 K),[43,84,85] while that of HNO_2 also differs by a factor of 2–3 with experimental values (3.7×10^{-1}–4.8×10^{-1} mol/m^3 Pa at 298 K).[86−88] The value of H_s^{cp} of N_2O_4 is lower than the experimental values[43,89,90] by an order of magnitude (1.4×10^{-3}–3.1×10^{-3} mol/m^3 Pa at 298 K). It should be noted that experimental measurement of H_s^{cp} for species that react with water is inherently difficult, as gas–liquid systems may not be maintained at equilibrium during measurement.[87]

The values of $\ln[K]$ of the reactions R2 and R4 at 273, 298, 313, and 333 K are calculated using the procedure described in Section 2.4 and are presented in Table 5. Since the HNO_2 dissociation to form nitrite and hydronium ions is well studied and documented, we calculated the value of $\ln[K]$ for reaction R3 using the reported value of pK_a in literature, where pK_a is the negative logarithm to the base ten of the acid dissociation constant (K_a). We used a value of 3.29[44] for the pK_a of HNO_2. The relation between $\ln[K]$ and pK_a is

$$\ln[K] = -\ln[10]\, pK_a - \ln[55.55] \quad (21)$$

The derivation of eq 21 is presented in the Supporting Information. The values of $\ln[K]$ of reactions R3 and R4 increase with increasing temperature, indicating more formation of reaction products with increasing temperature. The value of $\ln[K]$ of reaction R2 decreases with increasing temperature, leading to lower formation of reaction products with increasing temperature. This shows that reaction R2 is an exothermic reaction, which is in agreement with existing experimental and computational works.[46,48]

Table 5. Values of $\ln[K]$ for Reactions R2, R3, and R4 at Different Temperatures[a]

$\ln[K]$	273 K	298 K	313 K	333 K
R2	$3.7_{0.1}$	$1.4_{0.2}$	$0.0_{0.1}$	$-1.38_{0.08}$
R3	−11.986	−11.599	−11.396	−11.154
R4	$-26.3_{0.3}$	$-25.9_{0.4}$	$-25.7_{0.2}$	$-25.4_{0.1}$

[a]Note that $\ln[K]$ for reactions R2 and R4 were computed using CASpy while for reaction R3, the values of $\ln[K]$ were taken from ref 83. The evaluation of the uncertainties in $\ln[K]$ for reactions R2 and R4 is discussed in Section 2.4.

Table 4. Computed Values of Henry Coefficients (H_s^{cp}) in Units of Mol/(m^3 Pa) for the Species Studied in This Work Using the TIP3P Water Model[37] for Different Temperatures[a]

T/[K]	$H_2O/[10^1]$	$NO_2/[10^{-5}]$	$N_2O_4/[10^{-3}]$	$HNO_2/[10^{-1}]$	$NO/[10^{-5}]$
273	$6.2_{0.2}$	$4.9_{0.1}$	8.7_{1}	$5.1_{0.4}$	$1.70_{0.07}$
298	$1.26_{0.04}$	$3.43_{0.07}$	$3.2_{0.3}$	$1.7_{0.2}$	$1.45_{0.03}$
313	$0.56_{0.02}$	$3.05_{0.06}$	$2.2_{0.3}$	$0.93_{0.07}$	$1.44_{0.02}$
333	$0.22_{0.003}$	$2.75_{0.06}$	$1.26_{0.06}$	$0.51_{0.02}$	$1.48_{0.02}$

[a]The standard deviations are given in subscripts.

https://doi.org/10.1021/acs.jctc.5c01718
J. Chem. Theory Comput. 2026, 22, 528−539

The gas phase equilibrium constant (K_p) determines the gas phase composition of the system. The number of NO_2 and N_2O_4 molecules in the gas phase as a function of total gas pressure (P_{total}) and temperature (T) are calculated using eq 13, and are presented in Table S10 of the Supporting Information. Note that the total gas pressure (P_{total}) in our system is the sum of the partial pressures of NO_2 (P_{NO_2}) and N_2O_4 ($P_{N_2O_4}$). For a given P_{total}, the concentration of NO_2 in the gas phase increases and the dimer concentration decreases with increasing temperature. In contrast, increasing P_{total} at a given temperature leads to a higher dimer concentration and a lower concentration of NO_2.

The speciations in the aqueous phase of the system are determined by the composition of the gas phase and the values of $\ln[K]$ of the reactions in the aqueous phase. The speciations in the aqueous phase of the system at different pressures and temperatures are presented in Figures 4, 5, and 6.

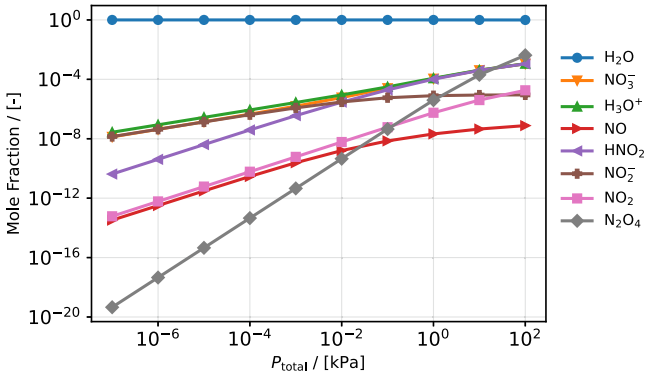

Figure 4. Mole fractions of species in the aqueous phase as a function of total gas pressure (P_{total}) at 298 K.

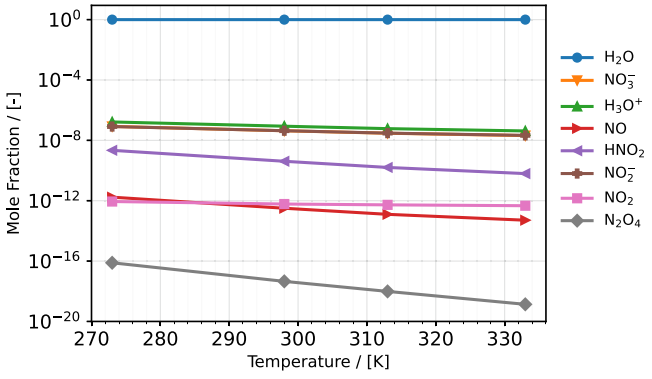

Figure 5. Mole fractions of species in the aqueous phase as a function of temperature at total gas pressure (P_{total}) of 10^{-6} kPa.

The mole fractions of the species as a function of P_{total} at 298 K are shown in Figure 4. The mole fractions of the species as a function of P_{total} at 273 K, 313 and 333 K are presented in Figures S11, S12 and S13 of the Supporting Information, respectively. The mole fractions of the species are also listed in Tables S11−S14 of the Supporting Information. The aqueous concentrations of all species, except water, increase by increasing P_{total} from 10^{-7} to 10^{2} kPa. The concentration of water decreases with increasing P_{total} as the increase of the concentration of NO_2 in the system leads to the equilibrium of reaction R2 being shifted further toward the reaction products, and therefore a lower concentration of water. Nitrate (NO_3^-) and nitrite (NO_2^-) ions have similar concentrations until 10^{-3} kPa, after which the difference in concentrations increases with increasing pressure. The concentration of hydronium ions (H_3O^+) is equal to the sum of the concentrations of NO_3^- and NO_2^- to satisfy the charge neutrality of the system. The concentration of nitrous acid (HNO_2) has a steady increase with P_{total}. The concentration of nitric oxide (NO) also has a steady increase with P_{total} until 10^{-2} kPa, after which the increase in the concentration tapers off.

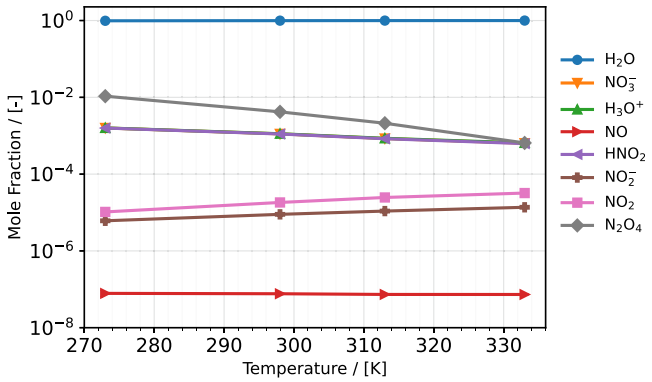

Figure 6. Mole fractions of species in the aqueous phase as a function of temperature at total gas pressure (P_{total}) of 10^2 kPa.

The equilibrium of reaction R4 is shifted to the reactant side as the value of $\ln[K]$ for reaction R4 is much negative (values of $\ln[K]$ range from −26.26 at 273 K to −25.41 at 333 K). This is in agreement with the work of Menezes & Popowicz[46] who reported that the dissociation reaction of HNO_2 to form NO_3^-, H_3O^+ and NO, is not thermodynamically favorable below 400 K. The pH of the system decreases with increasing pressure as a result of the increase in the presence of nitric and nitrous acids.

Figures 5 and 6 show the mole fractions of species in the aqueous phase as a function of temperature at a total gas pressure (P_{total}) of 10^{-6} kPa and 10^2 kPa, respectively. The data is listed in Tables S15 and S16 of the Supporting Information. The concentrations of the species in the aqueous phase decrease with increasing temperature, except for water. The concentration of water increases because with increasing temperature, the $\ln[K]$ of reaction R2 decreases, indicating a shift in the reaction equilibrium to the reactant side. A shift of the equilibrium reaction of R2 toward the reactant side should translate to more NO_2 concentration in the aqueous phase. The decreasing solubility of nitrogen dioxide with increasing temperature leads to an overall decrease in the aqueous concentration of the species with temperature, especially at lower values of P_{total} (<10 kPa). At higher P_{total} (≥10 kPa), there is an increased presence of NO_2 dimers (N_2O_4) in the solution (as also reported in experimental works[84]), which tend to dissociate with increasing temperature, therefore increasing the NO_2 aqueous concentration with increasing temperature (see Table S16). The concentration of nitrite ions increases with temperature at P_{total} greater than 0.1 kPa.

The ratio between the mole fractions of NO_2^- and HNO_2 in the aqueous phase, $\frac{X_{NO_2^-}}{X_{HNO_2}}$, depends on the values of $\ln[K]$ of reaction R3. $\ln[K]$ of reaction R3 becomes more positive with increasing temperature. Therefore, it is expected to have an increase in $\frac{X_{NO_2^-}}{X_{HNO_2}}$ with increasing temperature. $\frac{X_{NO_2^-}}{X_{HNO_2}}$ increases

https://doi.org/10.1021/acs.jctc.5c01718
J. Chem. Theory Comput. 2026, 22, 528−539

from 3.75×10^{1} at 273 K to 1.06×10^{2} at 298 K for P_{total} of 10^{-6} kPa. However, by increasing pressure to 10^{2} kPa, $\frac{X_{NO_2^-}}{X_{HNO_2}}$ only increases from 3.83×10^{-3} at 273 K to 8.07×10^{-3} at 298 K. This is because the equilibrium of reaction R2 shifts toward the reaction products with an increase in the pressure (more NO_2 concentration), leading to a higher mole fraction of HNO_2. Figure 7 shows the total nitrogen content ($X_{N\text{-total}}$)

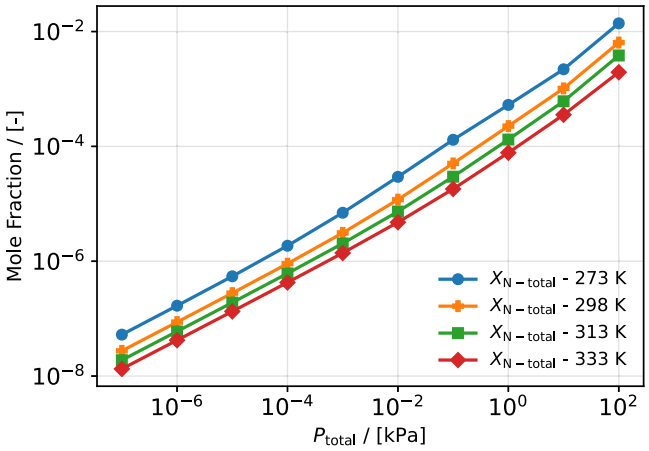

Figure 7. Sum of the mole fractions of nitrogen-containing species in the aqueous phase ($X_{N\text{-total}}$) as a function of total gas pressure (P_{total}) at 273 K, 298 K, 313 and 333 K.

present in the system as a function of the total pressure for four different temperatures. $X_{N\text{-total}}$ increases with increasing pressure and decreases with increasing temperature.

We would like to emphasize the importance of accurate data for parameters such as the atomization energy (D_0) of the species. The atomization energy of a species contributes considerably to the determination of the chemical equilibrium of the reaction. The chemical accuracy of ab initio calculations, which are used to determine the value of D_0 of species, is 4.184 kJ/mol.[91] This variance in the atomization energy contributes to differences in the reaction equilibrium constant. For example, we varied the atomization energy of NO within the chemical precision, and we found that $\ln[K]$ is different by 3.2 $\ln[K]$ points for reaction R4. The different values of atomization energies that are used in different studies ultimately lead to different results. Another important parameter is the value of the electron affinity of NO_3, which is used to calculate the atomization energy of NO_3^-. Although we have used a value of 3.09 eV, the reported values in the literature vary from 2.48 eV[82] to 3.94 eV.[92] Therefore, depending on the values of the atomization energies and electron affinities of the species, the reaction equilibrium could shift toward reactants or the reaction products.

4. CONCLUSIONS

We studied the interaction of NO and NO_2 with water. NO was modeled using the Saji FF, and the thermodynamic properties were computed using MD and CFCMC simulations. The self-diffusion coefficients of NO in water were calculated in water containing mole fractions of 0.005, 0.015, and 0.025 NO at temperatures ranging from 273 K−333 K. The values of self-diffusion coefficients are in good agreement with the experimental values. The Henry coefficient of NO was computed for temperatures ranging from 273 K−333 K. Experimental values are only available at 298 K, and the computed Henry coefficient at 298 K is in agreement with the experimental ones. The interaction of NO_2 in water is characterized by the initial hydrolysis of NO_2 to form nitrous and nitric acids, the subsequent ionization reaction of nitrous acid to form nitrate and hydronium ions and the disproportionation reaction of nitrous acid to form nitric acid, nitric oxide and water. We modified the CASpy solver, a chemical reaction equilibrium solver, to handle arbitrary constraints in chemical reaction equilibria, to study this interaction. The values of μ^{ex} of the species involved in the reactions are required as input in CASpy, and were computed using CFCMC simulations. Since NO_2 dimerizes to form N_2O_4, the gas phase composition at different pressures and temperatures must be calculated using the gas phase equilibrium constant. The calculation shows that the concentration of N_2O_4 in the gas phase increases with increasing pressure and decreases with increasing temperature. The equilibrium of reaction for the hydrolysis of NO_2 in water shifts to the reactant side with an increase in temperature, indicating that this reaction is an exothermic reaction. The composition in the aqueous phase as a function of pressure is computed. All species except water have an increase in their aqueous concentrations with increasing pressure, while that of water decreases. The pH of the system decreases with increasing pressure as the amount of nitrous and nitric acids increases. The speciations as a function of temperature are also computed. The aqueous concentrations of all species other than water decrease with increasing temperature. At higher pressures, the concentrations of NO_2 and NO_2^- also increases with increasing temperature. The ratio between the aqueous mole fractions of NO_2^- and HNO_2 increases with increasing temperature as the equilibrium of reaction R3 shifts toward the reaction products with an increase in temperature. We also discussed the importance of accurate data for parameters such as the atomization energy for calculating the reaction equilibrium. This work assumes thermodynamic equilibrium and does not include kinetic pathways or transport limitations. Future extensions could integrate reaction dynamics or interface-specific effects.

■ ASSOCIATED CONTENT

Supporting Information

The Supporting Information is available free of charge at https://pubs.acs.org/doi/10.1021/acs.jctc.5c01718.

Schematic representations of the species studied in this work and their geometries are presented in Figures S1−S7; The parameters of potential energy functions for NO_2, N_2O_4, H_3O^+, NO_2^-, NO_3^-, HNO_2 and NO are provided in Tables S1−S8; The inputs required to calculate the isolated molecule partition functions of the species involved in the system are provided in Table S9; Table S10 contains the gas phase composition as a function of temperature and pressure; The mole fractions of the species as a function of the total gas pressure at four different temperatures are provided in Tables S11−S14; The mole fractions of the species as a function of temperature at total gas pressures of 10^{-6} kPa and 10^{2} kPa are provided in Tables S15 and S16, respectively; Table S17 contains the means and standard deviations of the mole fractions of species obtained using error propagation analysis at 273 K and at a total gas pressure of 10^{1} kPa; The following derivations are

https://doi.org/10.1021/acs.jctc.5c01718
J. Chem. Theory Comput. 2026, 22, 528−539

provided: the relation between $\ln[K]$ and the acid dissociation constant, the calculation of mass balances that are required as input in CASpy, the dimerization constant in the gas phase, and the analytical expression that is used to obtain the gas phase composition; Figure S8 shows the self-diffusion coefficients of water in NO-water systems for different concentrations of NO at different temperatures; Figure S9 shows the viscosities of NO-water systems for different concentrations of NO at different temperatures; Figure S10 shows the comparison of harmonic and cosine-based angle potential functions for HNO_2 molecule; The mole fractions of the species in the aqueous phase of the NO_2-water system as a function of the total gas pressure for three different temperatures are shown in Figures S11−S13; In Figures S14 and S15, the probability distribution as a function of $\ln[K]$ and mole fraction of species at 273 K at a total gas pressure of 10^1 kPa are shown as histograms together with their corresponding fits to a Gaussian distribution; Figure S16 shows $\left\langle \frac{\partial U}{\partial \lambda} \right\rangle$ as a function of λ along with the corresponding cubic spline fit for the NO_3^- + H_3O^+ system at 298 K; The CASpy solver that includes our added functionality can be found here: https://github.com/omoultosEthTuDelft/CASpy/tree/Version-2.0/src/CASpy_ReactionEquilibria; The Python script that was used to calculate the values μ^{ex} for the NO_3^- + H_3O^+ system using thermodynamic integration can be found here https://github.com/tijinsaji/PhD-TU-e/tree/main; The inputs for running the CFCMC and MD simulations are provided at https://zenodo.org/doi/10.5281/zenodo.17866551 (PDF)

AUTHOR INFORMATION

Corresponding Author

Behnaz Bagheri − *Department of Applied Physics and Science Education, Technical University of Eindhoven, Eindhoven 5600 MB, The Netherlands; Institute for Complex Molecular Systems, Eindhoven 5600 MB, The Netherlands;* orcid.org/0000-0003-0887-5074; Email: b.bagheri@tue.nl

Authors

Tijin H. G. Saji − *Department of Applied Physics and Science Education, Technical University of Eindhoven, Eindhoven 5600 MB, The Netherlands; Institute for Complex Molecular Systems, Eindhoven 5600 MB, The Netherlands*

Thijs J. H. Vlugt − *Process & Energy Department, Faculty of Mechanical, Maritime and Materials Engineering, Delft University of Technology, Delft 2628 CB, The Netherlands;* orcid.org/0000-0003-3059-8712

Sofia Calero − *Department of Applied Physics and Science Education, Technical University of Eindhoven, Eindhoven 5600 MB, The Netherlands;* orcid.org/0000-0001-9535-057X

Complete contact information is available at: https://pubs.acs.org/10.1021/acs.jctc.5c01718

Author Contributions

All authors conceived the work. TS carried out the simulations and data analysis. All authors provided critical feedback on the interpretation of the data analysis. TS and BB prepared the manuscript in collaboration with TV and SC.

Notes

The authors declare no competing financial interest.

ACKNOWLEDGMENTS

TS thanks the Institute for Complex Molecular Systems for financial support.

REFERENCES

(1) Kim, H. H. Nonthermal plasma processing for air-pollution control: a historical review, current issues, and future prospects. *Plasma Processes Polym.* **2004**, *1*, 91−110.

(2) Laroussi, M. From Killing Bacteria to Destroying Cancer Cells: 20 Years of Plasma Medicine. *Plasma Process. Polym.* **2014**, *11*, 1138−1141.

(3) Von Woedtke, T.; Metelmann, H.-R.; Weltmann, K.-D. Clinical plasma medicine: state and perspectives of in vivo application of cold atmospheric plasma. *Contrib. Plasma Phys* **2014**, *54*, 104−117.

(4) Perni, S.; Shama, G.; Kong, M. G. Cold atmospheric plasma disinfection of cut fruit surfaces contaminated with migrating microorganisms. *J. Food Prot.* **2008**, *71*, 1619−1625.

(5) Schlüter, O.; Ehlbeck, J.; Hertel, C.; Habermeyer, M.; Roth, A.; Engel, K.-H.; Holzhauser, T.; Knorr, D.; Eisenbrand, G. Opinion on the use of plasma processes for treatment of foods. *Mol. Nutr. Food Res.* **2013**, *57*, 920−927.

(6) Puač, N.; Gherardi, M.; Shiratani, M. Plasma agriculture: A rapidly emerging field. *Plasma Processes Polym.* **2018**, *15*, 1700174.

(7) Gaunt, L. F.; Beggs, C. B.; Georghiou, G. E. Bactericidal action of the reactive species produced by gas-discharge nonthermal plasma at atmospheric pressure: a review. *IEEE Trans. Plasma Sci* **2006**, *34*, 1257−1269.

(8) Bruggeman, P. J.; Kushner, M. J.; Locke, B. R.; Gardeniers, J. G. E.; Graham, W. G.; Graves, D. B.; Hofman-Caris, R. C. H. M.; Maric, D.; Reid, J. P.; Ceriani, E.; et al. Plasma−liquid interactions: a review and roadmap. *Plasma Sources Sci. Technol* **2016**, *25*, 053002.

(9) Foster, J. E. Plasma-based water purification: Challenges and prospects for the future. *Phys. Plasmas* **2017**, *24*, 055501.

(10) Graves, D. B. The emerging role of reactive oxygen and nitrogen species in redox biology and some implications for plasma applications to medicine and biology. *J. Phys. D: Appl. Phys.* **2012**, *45*, 263001−263043.

(11) Graves, D. B. Low temperature plasma biomedicine: A tutorial review. *Phys. Plasmas* **2014**, *21*, 080901.

(12) Lu, X.; Naidis, G. V.; Laroussi, M.; Reuter, S.; Graves, D. B.; Ostrikov, K. Reactive species in non-equilibrium atmospheric-pressure plasmas: Generation, transport, and biological effects. *Phys. Rep.* **2016**, *630*, 1−84.

(13) Wende, K.; Williams, P.; Dalluge, J.; Van Gaens, W.; Aboubakr, H.; Bischof, J.; Von Woedtke, T.; Goyal, S. M.; Weltmann, K.-D.; Bogaerts, A.; et al. Identification of the biologically active liquid chemistry induced by a nonthermal atmospheric pressure plasma jet. *Biointerphases* **2015**, *10*, 029518.

(14) Khlyustova, A.; Labay, C.; Machala, Z.; Ginebra, M.-P.; Canal, C. Important parameters in plasma jets for the production of RONS in liquids for plasma medicine: A brief review. *Front. Chem. Sci. Eng* **2019**, *13*, 238−252.

(15) Lindsay, A.; Byrns, B.; King, W.; Andhvarapou, A.; Fields, J.; Knappe, D.; Fonteno, W.; Shannon, S. Fertilization of radishes, tomatoes, and marigolds using a large-volume atmospheric glow discharge. *Plasma Chem. Plasma Process.* **2014**, *34*, 1271−1290.

(16) Bradu, C.; Kutasi, K.; Magureanu, M.; Puač, N.; Živković, S. Reactive nitrogen species in plasma-activated water: generation, chemistry and application in agriculture. *J. Phys. D: Appl. Phys.* **2020**, *53*, 223001−223021.

(17) Guo, D.; Liu, H.; Zhou, L.; Xie, J.; He, C. Plasma-activated water production and its application in agriculture. *J. Sci. Food Agric.* **2021**, *101*, 4891−4899.

(18) Verlackt, C.; Van Boxem, W.; Bogaerts, A. Transport and accumulation of plasma generated species in aqueous solution. *Phys. Chem. Chem. Phys.* **2018**, *20*, 6845−6859.
(19) Norberg, S. A.; Tian, W.; Johnsen, E.; Kushner, M. J. Atmospheric pressure plasma jets interacting with liquid covered tissue: touching and not-touching the liquid. *J. Phys. D: Appl. Phys.* **2014**, *47*, 475203.
(20) Tian, W.; Kushner, M. J. Atmospheric pressure dielectric barrier discharges interacting with liquid covered tissue. *J. Phys. D: Appl. Phys.* **2014**, *47*, 165201.
(21) Lindsay, A.; Anderson, C.; Slikboer, E.; Shannon, S.; Graves, D. Momentum, heat, and neutral mass transport in convective atmospheric pressure plasma-liquid systems and implications for aqueous targets. *J. Phys. D: Appl. Phys.* **2015**, *48*, 424007.
(22) Lindsay, A. D.; Graves, D. B.; Shannon, S. C. Fully coupled simulation of the plasma liquid interface and interfacial coefficient effects. *J. Phys. D: Appl. Phys.* **2016**, *49*, 235204.
(23) Lietz, A. M.; Kushner, M. J. Air plasma treatment of liquid covered tissue: long timescale chemistry. *J. Phys. D: Appl. Phys.* **2016**, *49*, 425204.
(24) Ikuse, K.; Hamaguchi, S. Roles of the reaction boundary layer and long diffusion of stable reactive nitrogen species (RNS) in plasma-irradiated water as an oxidizing media-numerical simulation study. *Jpn. J. Appl. Phys.* **2022**, *61*, 076002.
(25) Bonitz, M.; Filinov, A.; Abraham, J.-W.; Balzer, K.; Kählert, H.; Pehlke, E.; Bronold, F. X.; Pamperin, M.; Becker, M.; Loffhagen, D.; et al. Towards an integrated modeling of the plasma-solid interface. *Front. Chem. Sci. Eng* **2019**, *13*, 201−237.
(26) Sakiyama, Y.; Graves, D. B.; Chang, H.-W.; Shimizu, T.; Morfill, G. E. Plasma chemistry model of surface microdischarge in humid air and dynamics of reactive neutral species. *J. Phys. D: Appl. Phys.* **2012**, *45*, 425201−425219.
(27) Dorai, R.; Kushner, M. J. A model for plasma modification of polypropylene using atmospheric pressure discharges. *J. Phys. D: Appl. Phys.* **2003**, *36*, 666−685.
(28) Atkinson, R.; Baulch, D.; Cox, R.; Hampson Jr, R.; Kerr, J.; Rossi, M.; Troe, J. Evaluated kinetic and photochemical data for atmospheric chemistry: supplement VI. IUPAC subcommittee on gas kinetic data evaluation for atmospheric chemistry. *J. Phys. Chem. Ref. Data* **1997**, *26*, 1329−1499.
(29) Sathiamoorthy, G.; Kalyana, S.; Finney, W.; Clark, R.; Locke, B. Chemical reaction kinetics and reactor modeling of NO x removal in a pulsed streamer corona discharge reactor. *Ind. Eng. Chem. Res.* **1999**, *38*, 1844−1855.
(30) Hao, X.; Mattson, A. M.; Edelblute, C. M.; Malik, M. A.; Heller, L. C.; Kolb, J. F. Nitric oxide generation with an air operated non-thermal plasma jet and associated microbial inactivation mechanisms. *Plasma Processes Polym.* **2014**, *11*, 1044−1056.
(31) Suschek, C. V.; Opländer, C. The application of cold atmospheric plasma in medicine: The potential role of nitric oxide in plasma-induced effects. *Clin. Plasma Med* **2016**, *4*, 1−8.
(32) Butenko, A. V.; Shekhter, A. B.; Pekshev, A. V.; Vagapov, A. B.; Fayzullin, A. L.; Serejnikova, N. B.; Sharapov, N. A.; Zaborova, V. A.; Vasilets, V. N. Review of clinical applications of nitric oxide-containing air-plasma gas flow generated by Plason device. *Clin. Plasma Med* **2020**, *19*, 100112−100120.
(33) Shi, W.; Maginn, E. J. Continuous Fractional Component Monte Carlo: An Adaptive Biasing Method for Open System Atomistic Simulations. *J. Chem. Theory Comput.* **2007**, *3*, 1451−1463.
(34) Shi, W.; Maginn, E. J. Improvement in molecule exchange efficiency in Gibbs ensemble Monte Carlo: Development and implementation of the continuous fractional component move. *J. Comput. Chem.* **2008**, *29*, 2520−2530.
(35) Rahbari, A.; Hens, R.; Ramdin, M.; Moultos, O.; Dubbeldam, D.; Vlugt, T. J. H. Recent advances in the Continuous Fractional Component Monte Carlo methodology. *Mol. Simul.* **2021**, *47*, 804−823.
(36) Saji, T. H. G.; Vlugt, T. J. H.; Calero, S.; Bagheri, B. Modeling nitric oxide and its dimer: force field development and thermodynamics of dimerization. *Phys. Chem. Chem. Phys.* **2025**, *27*, 13662−13674.
(37) Jorgensen, W. L.; Chandrasekhar, J.; Madura, J. D.; Impey, R. W.; Klein, M. L. Comparison of simple potential functions for simulating liquid water. *J. Chem. Phys.* **1983**, *79*, 926−935.
(38) Abascal, J. L.; Vega, C. A general purpose model for the condensed phases of water: TIP4P/2005. *J. Chem. Phys.* **2005**, *123*, 234505.
(39) Wise, D.; Houghton, G. Diffusion coefficients of neon, krypton, xenon, carbon monoxide and nitric oxide in water at 10−60°C. *Chem. Eng. Sci.* **1968**, *23*, 1211−1216.
(40) Zacharia, I. G.; Deen, W. M. Diffusivity and solubility of nitric oxide in water and saline. *Ann. Biomed. Eng.* **2005**, *33*, 214−222.
(41) Malinski, T.; Taha, Z.; Grunfeld, S.; Patton, S.; Kapturczak, M.; Tomboulian, P. Diffusion of nitric oxide in the aorta wall monitored in situ by porphyrinic microsensors. *Biochem. Biophys. Res. Commun.* **1993**, *193*, 1076−1082.
(42) Zafiriou, O. C.; McFarland, M. Determination of trace levels of nitric oxide in aqueous solution. *Anal. Chem.* **1980**, *52*, 1662−1667.
(43) Komiyama, H.; Inoue, H. 20 Absorption of nitrogen oxides into water. *Chem. Eng. Sci.* **1980**, *35*, 154−161.
(44) Schwartz, S. E.; White, W. H. Kinetics of reactive dissolution of nitrogen oxides into aqueous solution. *Adv. Environ. Sci. Technol.* **1983**, *12*, 1−116.
(45) Tan, S. P.; Piri, M. Modeling the solubility of nitrogen dioxide in water using perturbed-chain statistical associating fluid theory. *Ind. Eng. Chem. Res.* **2013**, *52*, 16032−16043.
(46) Menezes, F.; Popowicz, G. M. Acid rain and flue gas: quantum chemical hydrolysis of NO_2. *ChemPhysChem* **2022**, *23*, No. e202200395.
(47) Finlayson-Pitts, B.; Wingen, L.; Sumner, A.; Syomin, D.; Ramazan, K. The heterogeneous hydrolysis of NO_2 in laboratory systems and in outdoor and indoor atmospheres: An integrated mechanism. *Phys. Chem. Chem. Phys.* **2003**, *5*, 223−242.
(48) England, C.; Corcoran, W. H. Kinetics and mechanisms of the gas-phase reaction of water vapor and nitrogen dioxide. *Ind. Eng. Chem. Fundam.* **1974**, *13*, 373−384.
(49) Hoinkis, N.; Litter, M. I. Mechanisms of sonochemical transformation of nitrate and nitrite under different conditions: Influence of additives and pH. *Ind. Eng. Chem. Res.* **2022**, *61*, 16408−16417.
(50) Yost, D. M. *Systematic Inorganic Chemistry*; Read Books, 2007, p440.
(51) Polat, H. M.; de Meyer, F.; Houriez, C.; Moultos, O. A.; Vlugt, T. J. H. Solving Chemical Absorption Equilibria using Free Energy and Quantum Chemistry Calculations: Methodology, Limitations, and New Open-Source Software. *J. Chem. Theory Comput.* **2023**, *19*, 2616−2629.
(52) Levine, J. S.; Augustsson, T. R.; Andersont, I. C.; Hoell, J. M.; Brewer, D. A. Tropospheric sources of NOx: Lightning and biology. *Atmos. Environ.* **1984**, *18* (9), 1797−1804.
(53) Verma, S.; Yadava, P. K.; Lal, D.; Mall, R.; Kumar, H.; Payra, S. Role of lightning NOx in ozone formation: A review. *Pure Appl. Geophys.* **2021**, *178*, 1425−1443.
(54) Holmes, C. D.; Bertram, T. H.; Confer, K. L.; Graham, K. A.; Ronan, A. C.; Wirks, C. K.; Shah, V. The role of clouds in the tropospheric NOx cycle: A new modeling approach for cloud chemistry and its global implications. *Geophys. Res. Lett.* **2019**, *46*, 4980−4990.
(55) Zhu, Z.; Xu, B. Purification technologies for NOx removal from flue gas: a review. *Separations* **2022**, *9*, 307−333.
(56) Lorentz, H. A. Über die Anwendung des Satzes vom Virial in der kinetischen Theorie der Gase. *Ann. Phys* **1881**, *248*, 127−136.
(57) Darden, T.; York, D.; Pedersen, L. Particle mesh Ewald: An N·log(N) method for Ewald sums in large systems. *J. Chem. Phys.* **1993**, *98*, 10089−10092.
(58) Essmann, U.; Perera, L.; Berkowitz, M. L.; Darden, T.; Lee, H.; Pedersen, L. G. A smooth particle mesh Ewald method. *J. Chem. Phys.* **1995**, *103*, 8577−8593.

https://doi.org/10.1021/acs.jctc.5c01718
J. Chem. Theory Comput. 2026, 22, 528−539

(59) Frenkel, D.; Smit, B. *Understanding Molecular Simulation: From Algorithms to Applications*, 3rd ed.; Elsevier, 2023.
(60) Bourasseau, E.; Lachet, V.; Desbiens, N.; Maillet, J.-B.; Teuler, J.-M.; Ungerer, P. Thermodynamic Behavior of the CO_2+ NO_2/N_2O_4 Mixture: A Monte Carlo simulation study. *J. Phys. Chem. B* **2008**, *112*, 15783−15792.
(61) Lasala, S.; Samukov, K.; Mert Polat, H.; Lachet, V.; Herbinet, O.; Privat, R.; Jaubert, J.-N.; Moultos, O. A.; De Ras, K.; J H Vlugt, T. Application of thermodynamics at different scales to describe the behaviour of fast reacting binary mixtures in vapour-liquid equilibrium. *Chem. Eng. J.* **2024**, *483*, 148961.
(62) Noroozi, J.; Smith, W. R. Force-Field-Based Computational Study of the Thermodynamics of a Large Set of Aqueous Alkanolamine Solvents for Post-Combustion CO_2 capture. *J. Chem. Inf. Model.* **2021**, *61*, 4497−4513.
(63) Cordeiro, R. M.; Yusupov, M.; Razzokov, J.; Bogaerts, A. Parametrization and Molecular Dynamics Simulations of Nitrogen Oxyanions and Oxyacids for Applications in Atmospheric and Biomolecular Sciences. *J. Phys. Chem. B* **2020**, *124*, 1082−1089.
(64) Hens, R.; Rahbari, A.; Caro-Ortiz, S.; Dawass, N.; Erdős, M.; Poursaeidesfahani, A.; Salehi, H. S.; Celebi, A. T.; Ramdin, M.; Moultos, O. A.; Dubbeldam, D.; Vlugt, T. J. H. Brick-CFCMC: Open Source Software for Monte Carlo Simulations of Phase and Reaction Equilibria Using the Continuous Fractional Component Method. *J. Chem. Inf. Model.* **2020**, *60*, 2678−2682.
(65) Polat, H. M.; Salehi, H. S.; Hens, R.; Wasik, D. O.; Rahbari, A.; de Meyer, F.; Houriez, C.; Coquelet, C.; Calero, S.; Dubbeldam, D.; Moultos, O. A.; Vlugt, T. J. H. New Features of the Open Source Monte Carlo Software Brick-CFCMC: Thermodynamic Integration and Hybrid Trial Moves. *J. Chem. Inf. Model.* **2021**, *61*, 3752−3757.
(66) Saji, T. H. G.; Vicent-Luna, J. M.; Vlugt, T. J. H.; Calero, S.; Bagheri, B. Computing solubility and thermodynamic properties of H_2O_2 in water. *J. Mol. Liq.* **2024**, *401*, 124530−124540.
(67) Thompson, A. P.; Aktulga, H. M.; Berger, R.; Bolintineanu, D. S.; Brown, W. M.; Crozier, P. S.; In't Veld, P. J.; Kohlmeyer, A.; Moore, S. G.; Nguyen, T. D.; et al. LAMMPS-a flexible simulation tool for particle-based materials modeling at the atomic, meso, and continuum scales. *Comput. Phys. Commun.* **2022**, *271*, 108171.
(68) Polyak, B. T. The conjugate gradient method in extremal problems. *USSR Comput. Math. Math. Phys* **1969**, *9*, 94−112.
(69) Jamali, S. H.; Wolff, L.; Becker, T. M.; De Groen, M.; Ramdin, M.; Hartkamp, R.; Bardow, A.; Vlugt, T. J. H.; Moultos, O. A. OCTP: A tool for on-the-fly calculation of transport properties of fluids with the order-n algorithm in LAMMPS. *J. Chem. Inf. Model.* **2019**, *59*, 1290−1294.
(70) Nosé, S. A unified formulation of the constant temperature molecular dynamics methods. *J. Chem. Phys.* **1984**, *81*, 511−519.
(71) Hoover, W. G. Canonical dynamics: Equilibrium phase-space distributions. *Phys. Rev. A* **1985**, *31*, 1695−1697.
(72) Yeh, I.-C.; Hummer, G. System-size dependence of diffusion coefficients and viscosities from molecular dynamics simulations with periodic boundary conditions. *J. Phys. Chem. B* **2004**, *108*, 15873−15879.
(73) Celebi, A. T.; Jamali, S. H.; Bardow, A.; Vlugt, T. J. H.; Moultos, O. A. Finite-size effects of diffusion coefficients computed from molecular dynamics: a review of what we have learned so far. *Mol. Simul.* **2021**, *47*, 831−845.
(74) Wang, F.; Landau, D. P. Efficient, Multiple-Range Random Walk Algorithm to Calculate the Density of States. *Phys. Rev. Lett.* **2001**, *86*, 2050−2053.
(75) Poursaeidesfahani, A.; Torres-Knoop, A.; Dubbeldam, D.; Vlugt, T. J. H. Direct free energy calculation in the Continuous Fractional Component Gibbs ensemble. *J. Chem. Theory Comput.* **2016**, *12*, 1481−1490.
(76) Salehi, H. S.; Hens, R.; Moultos, O. A.; Vlugt, T. J. H. Computation of gas solubilities in choline chloride urea and choline chloride ethylene glycol deep eutectic solvents using Monte Carlo simulations. *J. Mol. Liq.* **2020**, *316*, 113729−113738.
(77) Sander, R. Compilation of Henry's law constants (version 4.0) for water as solvent. *Atmos. Chem. Phys.* **2015**, *15*, 4399−4981.
(78) Matito-Martos, I.; Rahbari, A.; Martin-Calvo, A.; Dubbeldam, D.; Vlugt, T. J. H.; Calero, S. Adsorption equilibrium of nitrogen dioxide in porous materials. *Phys. Chem. Chem. Phys.* **2018**, *20*, 4189−4199.
(79) Vegh, A.; Korozs, J.; Kaptay, G. Extension of the Gibbs−Duhem equation to the partial molar surface thermodynamic properties of solutions. *Langmuir* **2022**, *38*, 4906−4912.
(80) Chase, M. W. *NIST-JANAF Thermochemical Tables*; American Chemical Society: Washington, DC; New York, 1998.
(81) Linstrom, P. J.; Mallard, W. G. The NIST Chemistry WebBook: A chemical data resource on the internet. *J. Chem. Eng. Data* **2001**, *46*, 1059−1063.
(82) Berkowitz, J.; Chupka, W.; Gutman, D. Electron affinities of O_2, O_3, NO, NO_2, NO_3 by endothermic charge transfer. *J. Chem. Phys.* **1971**, *55*, 2733−2745.
(83) Seinfeld, J. H.; Pandis, S. N. *Atmospheric Chemistry and Physics: From Air Pollution to Climate Change*; John Wiley & Sons, 2016.
(84) Cheung, J.; Li, Y.; Boniface, J.; Shi, Q.; Davidovits, P.; Worsnop, D.; Jayne, J.; Kolb, C. Heterogeneous interactions of NO_2 with aqueous surfaces. *J. Phys. Chem. A* **2000**, *104*, 2655−2662.
(85) Lee, Y.; Schwartz, S. Reaction kinetics of nitrogen dioxide with liquid water at low partial pressure. *J. Phys. Chem.* **1981**, *85*, 840−848.
(86) Becker, K. H.; Kleffmann, J.; Martin Negri, R.; Wiesen, P. Solubility of nitrous acid (HONO) in ammonium sulfate solutions. *J. Chem. Soc., Faraday Trans.* **1998**, *94*, 1583−1586.
(87) Park, J. Y.; Lee, Y. N. Solubility and decomposition kinetics of nitrous acid in aqueous solution. *J. Phys. Chem.* **1988**, *92*, 6294−6302.
(88) Komiyama, H.; Inoue, H. Reaction and transport of nitrogen oxides in nitrous acid solutions. *J. Chem. Eng. Jpn.* **1978**, *11*, 25−32.
(89) Komiyama, H.; Inoue, H. Absorption of nitrogen oxides into water. *Chem. Eng. Sci.* **1980**, *35*, 154−161.
(90) Kramers, H.; Blind, M.; Snoeck, E. D2. Absorption of nitrogen tetroxide by water jets. *Chem. Eng. Sci.* **1961**, *14*, 115−123.
(91) Zheng, P.; Yang, W.; Wu, W.; Isayev, O.; Dral, P. O. Toward chemical accuracy in predicting enthalpies of formation with general-purpose data-driven methods. *J. Phys. Chem. Lett.* **2022**, *13*, 3479−3491.
(92) Weaver, A.; Arnold, D.; Bradforth, S.; Neumark, D. Examination of the $^2A_2$ and $^2E''$ states of NO_3 by ultraviolet photoelectron spectroscopy of NO_3^-. *J. Chem. Phys.* **1991**, *94*, 1740−1751.

https://doi.org/10.1021/acs.jctc.5c01718
J. Chem. Theory Comput. 2026, 22, 528−539